The kinesin-8, Kip3, switches microtubule protofilaments in a sideward random walk asymmetrically biased by force

Michael Bugiel
Center for Plant Molecular Biology,
Universität Tübingen, Tübingen, Germany

Elisa Böhl
Center for Plant Molecular Biology,
Universität Tübingen, Tübingen, Germany

Erik Schäffer[1]
Cellular Nanoscience Group, Center for Plant Molecular Biology,
Universität Tübingen, Tübingen, Germany

March 11, 2015

[1]Corresponding author. Address: Center for Plant Molecular Biology (ZMBP), University of Tübingen, Auf der Morgenstelle 32, 72076 Tübingen, Germany, Tel.: +49(0)7071-29-78831

Abstract

Molecular motors translocate along cytoskeletal filaments such as kinesin motors on microtubules. While conventional kinesin-1 tracks a single microtubule protofilament, other kinesins, akin to dyneins, switch protofilaments. However, the molecular trajectory—whether protofilament switching occurs in a directed or stochastic manner—is unclear. Here, we used high-resolution optical tweezers to track the path of single budding yeast kinesin-8, Kip3, motor proteins. Under applied sideward loads, we found that individual motors stepped sideward in both directions with and against loads with a broad distribution in measured step sizes. Interestingly, the force response depended on the direction. Based on a statistical analysis and simulations accounting for the geometry, we propose a diffusive sideward stepping motion of Kip3 on the microtubule lattice, asymmetrically biased by force. This finding is consistent with previous multi-motor gliding assays and sheds light on the molecular switching mechanism. For kinesin-8, the diffusive switching mechanism may enable the motor to bypass obstacles and reach the microtubule end for length regulation. For other motors, such a mechanism may have implications for torque generation around the filament axis.

Key words: Kinesin; microtubules; microtubule depolymerase; optical tweezers; random walk

Introduction

Translocation of motor proteins along cytoskeletal filaments fulfills diverse cellular functions (1). For example, the dimeric kinesin-1 transports cargo by taking 8 nm steps in a hand-over-hand fashion along microtubules (2–5). Microtubules consist of circularly arranged protein chains, so-called protofilaments, assembled of α/β-tubulin dimers (1). Kinesin-1 tracks a single protofilament (6–8), seldom switching between them (9, 10). Sidewards motion of other motors have been detected via rotations of filaments driven by multiple motors in gliding assays and by off-axis movement of motor-attached microspheres or quantum dots used as tracking probes. Probe or microtubule rotations imply torque generation for all cytoskeletal motors: myosin (11), dynein (9, 12–17) and kinesin (kinesin-1: monomers (18) and dimers (10), kinesin-2 (19, 20), kinesin-5 (21), kinesin-8 (16, 22) kinesin-14 (23)). Occasional *directed* sideward steps—as suggested for kinesin-8—may explain microtubule rotations of motor-ensemble gliding assays (22) or the spiralling motion of multi-motor-coated microspheres around microtubules (20). However, motors may also *randomly* switch protofilaments with a bias towards one direction resulting in the same *net* ensemble motion. While data on single cytoplasmic dyneins suggest a diffusive, i.e. undirected, sideward stepping mechanism (15–17), the switching mechanism of single kinesin motors remains poorly understood. In both cases, how sideward stepping may depend on load is unclear.

To determine the switching mechanism for a kinesin motor, we investigated the translocation of the budding yeast kinesin-8, Kip3. Instead of transporting cargo, Kip3 depolymerizes microtubules and thereby regulates their dynamics and length (24–26). To do so, the motor needs to reach the microtubule end and thus, ideally, should have two features: (i) it should be highly processive—taking many steps without dissociating from the microtubule—and (ii) it should be able to bypass obstacles. While the high processivity of Kip3 with an average run length of up to 12 µm (24, 27) was shown to be due to a weakly bound slip state (28, 29), in addition to a second microtubule binding site at the motor's tail (27), the obstacle-bypassing capability has only been proposed (22). To bypass an obstacle, the motor should have the ability to switch microtubule protofilaments, as suggested by microtubule rotations seen in motor ensemble gliding assays (22). Here, we probed how protofilament switching occurs on the molecular level by applying alternating sideward loads on single, microsphere-coupled Kip3 motors using optical tweezers. In addition, we simulated the motion with force-dependent sideward stepping rates. Both the data and simulation are

consistent with a random sideward walk asymmetrically biased by force. The ability to side step suggests that Kip3 is well-suited to bypass obstacles on microtubules.

Materials and Methods

Microtubule preparation

Porcine tubulin was polymerized in BRB80 buffer (80 mM PIPES, 1 mM EGTA, 1 mM $MgCl_2$, pH = 6.9) with 5 % dimethyl sulfoxide (DMSO), 4 mM $MgCl_2$ and 1 mM GTP for 1 h at 37 °C. Afterwards, microtubules were diluted with BRB80 containing 10 μM taxol (BRB80T), spun down in a Beckmann airfuge and re-suspended in BRB80T. If not noted otherwise, all chemicals are from Sigma. Microtubules were visualized with differential interference contrast employing a light emitting diode (LED-DIC) (30).

Microsphere preparation

Motors were bound to microspheres via antibodies and a flexible polymer spacer. Carboxylated polystyrene microspheres (mean diameter 0.59 μm, Bangs Lab., Fishers, USA) were coated covalently with a 3 kDa polyethylene glycol (PEG) linker and a GFP antibody as described in (28, 31). The GFP antibody was expressed and purified in the protein expression facility of the Max Planck Institute for Molecular Cell Biology and Genetics (MPI CBG), Dresden, Germany.

Sample preparation and assay

Experiments were performed in flow cells that were constructed with silanized, hydrophobic cover slips as described in (32). The motor proteins budding yeast Kip3 (His_6-Kip3-eGFP) and rat kinesin-1 (His_6-rkin430-eGFP) were expressed and purified according to (28, 33). The motility buffer for Kip3 stepping assays is BRB80 supplemented with 1 mM ATP, casein, taxol, and an anti-fading mix (28). Motility buffer for assays with non-motile Kip3 contained 1 mM AMPPNP (Jena Bioscience, Germany) instead of ATP; motility buffers for kinesin-1 assays had 1–2 μM ATP. PEG microspheres were mixed with kinesins in motility buffer to a motor-microsphere ratio where every third microsphere showed motility implying single-molecule conditions with 95 % confidence (34). The channels of flow cells were washed with BRB80, filled and incubated for 20 min successively with anti

β-tubulin I (monoclonal antibody SAP.4G5 from Sigma in BRB80), Pluronic F-127 (1 % in BRB80) and microtubules in BRB80T. Finally, the kinesin-microsphere mix was flowed in.

Optical tweezers setup

Measurements were performed in a single beam optical tweezers setup as described in (29, 35, 36). It is equipped with a millikelvin precision temperature control, a lateral force feedback using piezo tilt mirrors and an axial force feedback using the sample stage with a feedback rate of 1 kHz. The trapping objective temperature was 29.2 °C. The optical trap is calibrated by analysis of the height-dependent power spectrum density as described in (35, 37).

Applying sideward loads with optical tweezers

The force clamp had a sampling rate of 4 kHz and a feedback rate of 1 kHz. The feedback parameters were tuned by using AMPPNP-bound Kip3 under single-molecule conditions and simulating 8 nm steps by moving the sample stage with a stepping rate of 5 Hz (corresponding to a velocity of 40 nm/s). In stepping assays, sideward loads of 0.5 pN were applied with a trap stiffness of 0.02–0.03 pN/nm and alternated every 1.75–20 s. No load was applied along the microtubule axis. Additionally, sideward loads of 0.25, 1, and 2.1 pN were applied for an alternating time of 5 s. The range of the force feedback was 3.5 µm, limiting our ability to determine the run length of the motor as a function of sideward load force. Data for forces and microsphere positions were smoothed with a running median filter for visualization. No data points from transients between the alternating loads were used for the analysis. As a measure for the overall sideward motion during alternating times, the y-position signal was fitted by a line; the difference between end and starting point of this fit has been taken as "sideward displacement" Δy. Means and variances were calculated; variances were averaged between different experiments. We preferentially used microtubules that were parallel to the flow cell channel coinciding with the x-axis of the detector and DIC camera image. The mean angle relative to this axis of all microtubules used in this work was $-2 \pm 7\,°$ (mean ± standard deviation). The microtubule angle was determined via image analysis with a precision of better than $1\,°$. Note that the force-feedback automatically tracked the microtubule axis. The recorded data were rotated by this measured angle. Occasionally, this rotation angle was fine-adjusted in the

MATLAB analysis to minimize any overall trend in the y-position signal. We determined the zero-position of the y-axis with a precision of ≈ 10 nm corresponding approximately to the rms noise on the position traces. For a typical 50 s long trace, this precision resulted in a systematic deviation of $(10/50 = 0.2)$ nm/s. For an alternating time of 20 s, the systematic deviation would be about $20\,\text{s} \times 0.2\,\text{nm}/2 = 4$ nm. Because we averaged data obtained from many different microtubules, the mean of the systematic deviations should be zero. The error on the rotation angle increased the variance of Δy—for the 20 s example it would be $16\,\text{nm}^2$, which is approximately equal to our measurement precision. For shorter alternating times, the effect is even smaller.

To ensure the functionality of the motors, we measured the speed of Kip3-coated microspheres by video tracking (30) with the optical trap turned off. We determined the speed by linear fits to the tracked x position. The speed was 40 ± 2 nm/s ($N = 52$, SEM if not noted otherwise), consistent with previous reports (24, 28, 29). With the trap turned on and no load applied in any direction (zero-force feedback), the speed was 39 ± 2 nm/s ($N = 90$, zero-force data point in Fig. 1C) ensuring that the trap and feedback did not affect the motor.

Results

Kip3 slowed down under off-axis loads

To measure sideward motion, we used optical tweezers (35–38) to precisely track the forward and sideward motion of single, microsphere-coupled Kip3 motors while subjected to sideward loads (Fig. 1A,B, see Materials and Methods). Kip3-coated microspheres were trapped and placed on taxol-stabilized microtubules. These microtubules have mostly 14 protofilaments and a mean supertwist of $\approx 8\,\mu$m (6). Using a force feedback, we applied no load along the microtubule axis and different—on average constant—sideward loads perpendicular to the microtubule axis. We define the motion along the axis of the microtubule to be in the x direction and off-axis, sideward motion to be in the y direction—left and right with respect to the forward direction corresponding to positive and negative y-values, respectively (Fig. 1B). Before investigating the sideward motion, we asked how sideward loads affect the forward translocation. During single Kip3 runs, we successively increased the sideward load while no load was applied along the microtubule axis. We found that the motor slowed down and

eventually detached at a mean force of $2.9 \pm 0.2\,\mathrm{pN}$ ($N = 31$, SEM if not noted otherwise) averaged over left and right (Fig. 1C). Detachment forces and slopes did not significantly depend on the pulling direction. Based on the extrapolated fits, motors stalled at a sideward load of about 4–5 pN. Note that due to the geometry, the sideward load (F_y) also causes an upward load (F_z) on the motor. We address the issue of the geometry in the simulation section below. The above results show that sideward loads moderately slowed down Kip3 compared to its $\approx 1\,\mathrm{pN}$ stall force on backward loads (28). However, in contrast to kinesin-1 (39), no significant asymmetry was observed with respect to the sideward pulling direction.
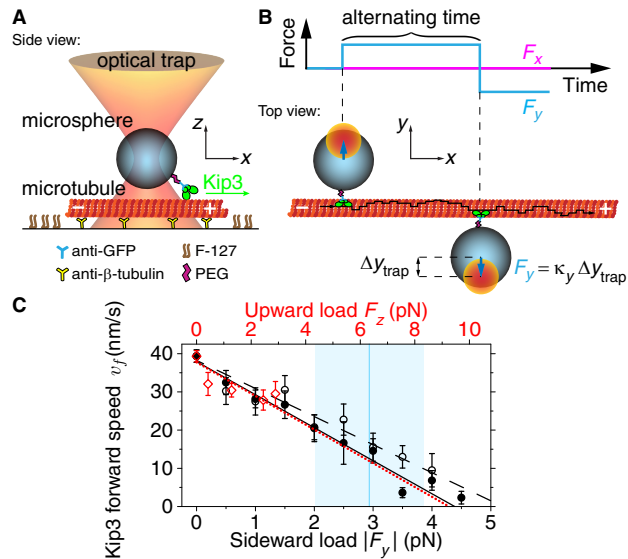
Fig. 1. Sideward loads slow down Kip3 motors. (*A*) Schematic side view of the stepping assay: A Kip3-coated microsphere is trapped with optical tweezers and placed on an immobilized microtubule. (*B*) Top view: A motor translocates towards the microtubule plus end (*x*-axis, black path) with no force applied in the direction of the microtubule axis. The motor is subjected to alternating, constant sideward loads of $F_y = \kappa_y \Delta y_{\mathrm{trap}}$ perpendicular to the microtubule axis (in the *y*-direction), where Δy_{trap} is the microsphere displacement from the trap center and κ_y the trap stiffness in the *y*-direction. Schematics not to scale. (*C*) Forward speed as a function of the absolute value of sideward (open and solid black circles for left and right, bottom axis) and upward (open red diamonds, top axis) load. Linear fits to the data are indicated by the lines. Dashed and solid black lines: sideward loads with slopes of $-8.6 \pm 0.6\,\mathrm{nm\,s^{-1}\,pN^{-1}}$ (SE, $N = 10$) and $-7.3 \pm 0.6\,\mathrm{nm\,s^{-1}\,pN^{-1}}$ ($N = 9$) for leftward and rightward loads, respectively; red dotted line: upward loads with a slope of $-4.1 \pm 1.2\,\mathrm{nm\,s^{-1}\,pN^{-1}}$ ($N = 5$). The vertical blue line indicates the mean detachment force and the blue shaded region its standard deviation.
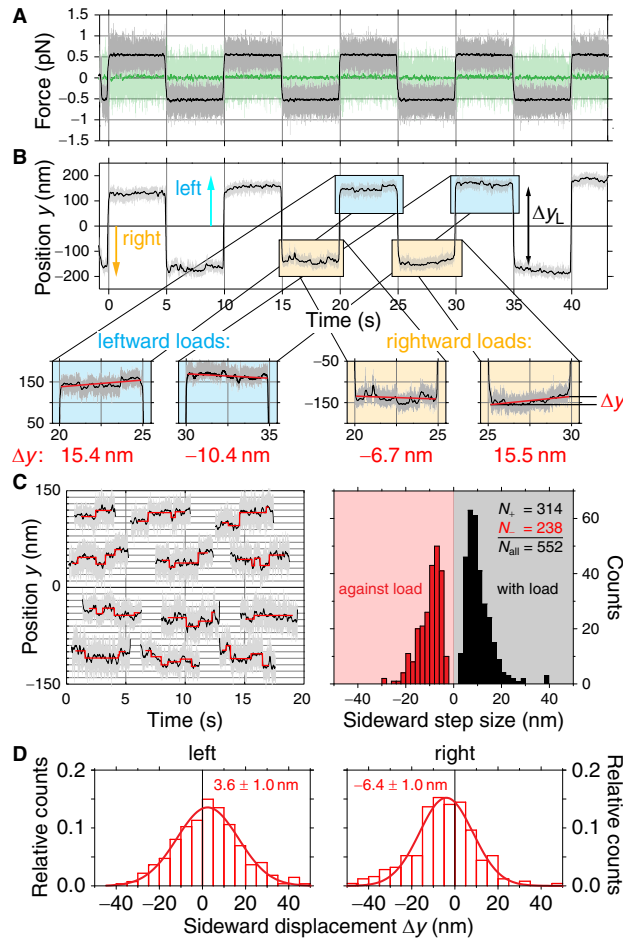
Fig. 2. Kip3-coupled microspheres moved sidewards with and against sideward loads. (*A*) Sideward load force as a function of time (gray line: raw data with 4 kHz, black line: median filtered to 8 Hz). Zero load was applied along the microtubule axis (light green line: raw data with 4 kHz, dark green line: median filtered to 8 Hz). (*B*) Sideward position y perpendicular to the microtubule axis as a function of time. Δy_L indicates the mean distance between the leftward- and rightward-pulled microsphere. Insets: Linear fits (blue lines) to the sideward motion resulted in the sideward displacement Δy indicated below the insets. (*C*) Left: Representative traces for left (positive y) and right, plotted together with detected steps (red lines). Traces are offset for clarity. Right: Histogram of detected step sizes for steps in the direction of or against the applied sideward load. (*D*) Histograms of sideward displacement Δy for leftward and rightward loads of 0.5 pN and an alternating time of 5 s (red bars). Gaussian fit (red line) and means±SEMs are indicated.

Single Kip3 motors switched protofilaments

To precisely measure the sideward motion of Kip3, we applied sideward loads of 0.5 pN perpendicular to the microtubule axis in the y-direction with no load along the microtubule axis (Fig. 1B, Fig. 2A). We regularly

changed the direction of the load from left to right with different alternating times and recorded the x and y position of the trapped microsphere as a function of time (see Materials and Methods). At 0.5 pN sideward load, the forward speed was 31.5 ± 0.6 nm/s ($N = 400$) corresponding to a forward stepping rate of $k_f \approx 4\,\mathrm{s}^{-1}$ for 8-nm steps (28) (Fig. 1C, Fig. S1 in the Supporting Material). In the sideward direction, there were large transient displacements Δy_L upon changing the load direction (Fig. 2B), which we attribute to the lever of the microsphere, motor and linker length. After the transient, small sideward displacements occurred during the constant-load time. We observed discrete sideward steps (Fig. 2C left). Our step finder (29) confidently detected a broad distribution of steps with and against load down to ≈3 nm and as large as 30 nm (see histogram Fig. 2C right) with a mean dwell time of ≈1 s (Fig. S2). To check for an asymmetry in the mean dwell times, in analogy to "limping" (3), we separately calculated the dwell times with or against load for left and right, respectively. We did not find a significant difference. Surprisingly, the largest detected step sizes are larger than the largest projected distance between protofilaments of ≈6 nm and even larger than the ≈25 nm diameter of a microtubule. We attribute the large *microsphere* steps to (i) the geometry (see simulation section below), (ii) the possibility of two fast subsequent steps, and (iii) the rms noise on the traces.

Because we could not detect all steps and the ones we could detect had a large, continuous variation in step sizes, we measured the sideward displacement Δy during the alternating time by a linear fit to the position traces *after* the transient (insets in Fig. 2B). For this fit-based sideward displacement, we also measured a broad distribution of both positive and negative sideward displacements independent of the loading direction with displacements again exceeding the microtubule diameter (red distributions in Fig. 2D). Interestingly, the mean values of the distribution significantly differed from zero: with a leftward and rightward load, there was a *small* mean displacement to the left and right, respectively, whereby the absolute value of the rightward displacement was larger. Together, these results suggest that Kip3 switched protofilaments in both directions and that the switching was asymmetrically biased by the loading force.

The variance of the sideward displacements increased with time

To determine whether protofilament switching was due to a directed or a random process, we varied the alternating time and determined the mean and variance of the sideward displacement distribution (see Fig. S3 for the
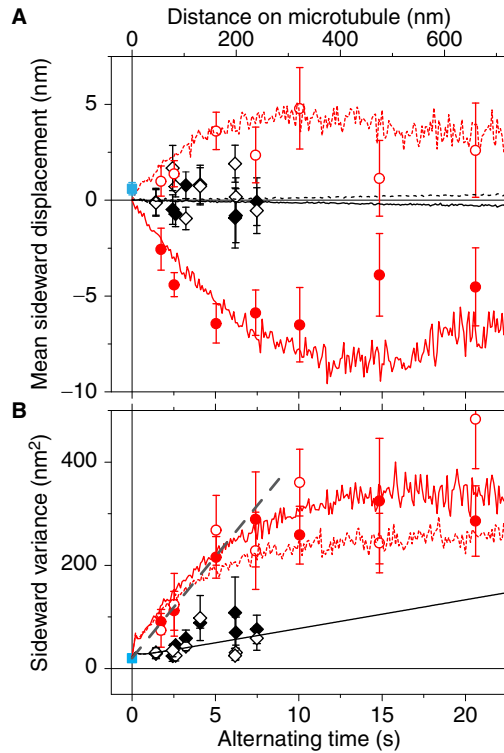
Fig. 3. Mean sideward displacement and variance increased with alternating time. (*A*) Mean sideward displacement (error bars are SEMs) and (*B*) variance as a function of alternating time with a sideward load of 0.5 pN for Kip3 (○ left and ● right), AMPPNP-bound Kip3 (■) and rkin430 (◇ left and ◆ right). Dashed and solid lines are the best-fit simulations for left and right, respectively (red: Kip3, black: rkin430). A linear fit (gray dashed line), $2Dt + 2\varepsilon^2$, to the first four variance data points including both directions for Kip3 resulted in a sideward diffusion coefficient quoted in the text and a measurement precision of $\varepsilon \approx 3$ nm.

histograms). The absolute mean sideward displacements for left and right (open and closed red circles in Fig. 3, respectively) first increased for alternating times less than about 10 s and then, within error bars, leveled off or slightly decreased (Fig. 3A). The initial increase was significantly larger than control measurements using (i) Kip3 in the presence of the non-hydrolyzable ATP analog adenosine 5'-(β,γ-imido)triphosphate (AMPPNP, blue solid square, Fig. S4A,C,D), (ii) kinesin-1 (open and solid black diamonds for left and right in Fig. 3, respectively, Fig. S5), or (iii) paused motors (Fig. S4B,E–H). The controls using kinesin-1 did not shown any dependence on the alternating time, either. Thus, for Kip3, the increase in the mean sideward displacement supports the notion that force biased the sideward stepping motion in the direction of the applied load.

For Kip3, the variances of the distributions increased with time while also leveling off for longer times (Fig. 3B). Compared to Kip3, the kinesin-1 data showed a much smaller increase (the initial slope is 7-fold smaller). For Kip3, the initial linear increase of the variance is reminiscent of a diffusive process. A linear fit (dashed gray line Fig. 3B) resulted in a sideward diffusion coefficient of $D = 20 \pm 2\,\mathrm{nm^2\,s^{-1}}$. We can use this diffusion coefficient to estimate the mean sideward stepping rate. To this end, we estimated the average projected distance between protofilaments on the top half of the microtubule to be $\langle \Delta p \rangle \approx 4\,\mathrm{nm}$ (Fig. S6A). With this estimate, the sideward stepping rate was $k_{\Delta p} = D/\langle \Delta p \rangle^2 \approx 1.3\,\mathrm{s^{-1}}$. Sideward movement due to the microtubule supertwist results in net sideward stepping rates, which are much smaller compared to this estimate. Therefore, the supertwist should not have a large influence on our measurements (see also Sect. S10). Taken together, the variance data for short alternating times is consistent with a random sideward walk. Yet, this simple analysis cannot account for the data at long alternating times and does not explain the broad distribution in sideward displacements and step sizes.

In addition to the alternating time, we varied the sideward load for an alternating time of 5 s (Fig. S7). The measurement revealed an increasing absolute mean sideward displacement with higher loads in both directions (Fig. S7A). The variance decreased up to 0.5 pN (Fig. S7B). For forces larger than 0.5 pN, the variance was larger. Based on video images, we attribute this large variance to insufficiently immobilized microtubules. In extreme cases, which were not used for data anlysis, microtubules were visibly displaced in the lateral direction for forces exceeding 0.5 pN.

A simulation accounting for the geometry supports an asymmetrically biased diffusion mechanism

To gain a deeper understanding of the observed data, we considered the experimental geometry to scale. In the above estimate for the sideward stepping rate, we tacitly assumed that the projected distance between protofilaments corresponds to the microsphere displacements that we measure. This assumption does not hold on close inspection of the geometry drawn to scale in Fig. 4A. The microsphere with radius R is held by the optical trap, which pulls the linker of length L between the microtubule of radius r and the microsphere taut. We assume that the microsphere does not change its distance h to the surface during the stepping motion of the motors. This assumption is supported by surface-force measurements (35) and the vertical displacements during the alternating time, which on average do not signif-
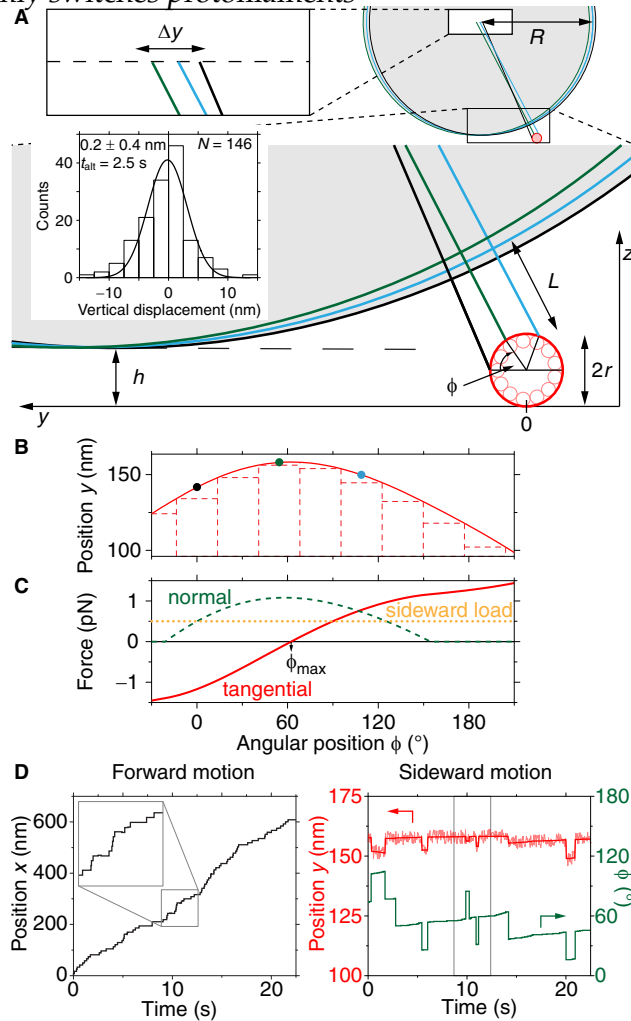
Fig. 4. Geometry to scale and simulated traces. (*A*) Geometry of microsphere (gray), linker and microtubule (red) with $R = 295$ nm, $L = 34$ nm (see Sects. S6,S9 and Fig. S9), $h = 20$ nm (35), and $r = 12.5$ nm drawn to scale. The different colors (black, green, blue) correspond to different angular motor positions. Upper inset: Magnification of microsphere center position. Lower inset: Histogram of vertical displacement Δz with mean±SEM and Gaussian fit for an alternating time of 2.5 s. (*B*) Microsphere position y as a function of angular motor position ϕ with a $360/13 \approx 28°$-grid to illustrate the various sideward step sizes between protofilaments. Colored points (black, green, blue) indicate the angular positions sketched in A. (*C*) Plot of the tangential (red solid line) and normal force (green dashed line) acting on Kip3 as a function of angular position ϕ relative to the applied sideward load (ocher dotted line). At the maximum microsphere position corresponding to the angle $\phi_{max} \approx 62°$, the tangential force is zero. (*D*) Typical simulated traces of forward (left panel), sideward (right panel, red line, left axis) motion of a Kip3-coupled microsphere along with the angular motor position (right, green line, right axis) and as a function of time. Inset: Magnification of forward steps showing small forward displacement at the times of sideward steps.

icantly differ from zero (lower inset Fig. 4A, Fig. S8). With this geometry, the lateral microsphere center position y can be calculated from the angular motor position ϕ on the microtubule (see Sect. S6 for an analytic expression

and Sect. S9 for other details of the geometry).

Figure 4B shows the non-linear dependence of the microsphere position $y(\phi)$ on the angular motor position ϕ. This function and the corresponding microsphere displacements upon sideward stepping are consistent with the large sideward displacements seen in the experiment (Fig. 2C,D). For the angular range shown in Fig. 4B, the difference between the maximum and minimum position is $\Delta y \approx 60$ nm. Thus, sideward *microsphere* displacements of up to 60 nm are possible even though the motor has only moved roughly the projected distance corresponding to the microtubule diameter of 25 nm. The geometry results in an amplified microsphere displacement compared to the motor displacement. For single steps, the microsphere displacements can continuously vary between -30 nm and $+40$ nm (Fig. S6B) consistent with the measured broad step-size distribution (Fig. 2C).

The function $y(\phi)$ is not monotonic, but has a maximum. This maximum results in a counterintuitive phenomenon: If in a gedanken experiment the motor starts at an angular position close to the maximum (green lines and position in Fig. 4A,B, respectively) and takes two clockwise angular steps to the right (blue lines and position in Fig. 4A,B), the microsphere center position also moves to the right (upper inset Fig. 4A). However, if the motor takes two counterclockwise angular steps to the left (black lines and position in Fig. 4A,B), the microsphere center position does not move to the left but also to the right. Thus, the microsphere movement may not reflect the angular directionality of the motor nor the projected distance between protofilaments. For the same reason, the directionality and magnitude of the force acting on the motor may differ from the applied load (Fig. 4C). Depending on the angular position of the motor, the force tangential to the microtubule cross section—corresponding to the sideward force in the reference frame of the motor (red solid line in Fig. 4C, Fig. S9)— can be more than twice the sideward load applied with the optical tweezers (ocher dotted line Fig. 4C) and also of opposite direction. Note that at the maximal displacement of the microsphere, the tangential force is zero and the normal force (green dashed line Fig. 4C) reaches a maximum. Using the relationship between microsphere position and angular motor position, we can re-estimate the sideward stepping rate. Based on the expected mean sideward stepping distance measured via the microsphere of $\approx 8.9 \pm 0.4$ nm (Fig. S6), the rate is $k_{\Delta y} = (0.30 \pm 0.06)\,\mathrm{s}^{-1}$, which is about 4× lower compared to the estimate based on the projected filament distance. Thus, the geometry leads to counterintuitive movement of the microsphere and does not allow for an analytical solution to describe our data.

To quantitatively describe all of our data, we simulated the sideward

stepping motion of the kinesin motors accounting for the geometry (see Sect. S11 for details). Because force biased the sideward motion, we simulated the motor translocation along the microtubule with Arrhenius-type, force-dependent sideward stepping rates

$$k_{l,r}(F_{\text{tang}}) = k_{l,r}^0 \exp\left[\pm F_{\text{tang}} \cdot x_{l,r}^\dagger / (k_B T)\right] \qquad (1)$$

where k_l^0 and k_r^0 are the zero-force sideward stepping rates towards the left and right (+ and − in the exponential, respectively), $x_{l,r}^\dagger$ are the distances to the transition states for the respective directions, F_{tang} is the tangential force acting on the motor, k_B the Boltzmann constant, and T the absolute temperature. Additionally, we accounted for the microtubule supertwist even though it had little influence on the results of the simulation (see Sect. S11 and Fig. S11). Furthermore, because the distance to the directly adjacent tubulin dimers is shortest (1, 22), we assumed that a sideward step is to one of the neighboring tubulin dimers (not diagonally to the front left or front right). The motor translocation was simulated and analyzed in the same manner as the experiments were performed. We simulated 200 traces consisting of the same number of alternating cycles as we acquired during the experiments for more than 100 000 sets of the sideward stepping parameters ($k_l^0, k_r^0, x_l^\dagger, x_r^\dagger$) as a function of alternating time. Then, we calculated the simulated mean and variance of the sideward displacement histograms. To account for the kinesin-1 variance increase, we added a global best-fit linear increase to both the simulated kinesin-1 and Kip3 variance. Subsequently, we calculated the mean-squared deviation of the simulated values from the experimental data normalized by the experimental error bars and number of degrees of freedom. In this manner, we determined a reduced χ_{red}^2-value for each set of simulated parameters.

The best-fit kinetic parameters corresponding to the simulation set with the smallest χ_{red}^2-value averaged over a simulation with and without variable supertwist are given in Table 1 (see Sects. S10,S11). Within error bars, the zero-force sideward stepping rates towards the left and right of $k_0 \approx 0.3\,\text{s}^{-1}$ did not differ. The distance to the transition states of $3.6 \pm 0.8\,\text{nm}$ and $2.5 \pm 1.0\,\text{nm}$ (SD, $N = 95$) for left and right, respectively, depended on the direction. Thus, in the absence of force, the simulation results support a purely diffusive sideward motion with a sideward stepping time of $\tau = (2k_0)^{-1} \approx 1.7\,\text{s}$. A directed process, i.e. with one of the rates being zero, does not describe our data well (see Figs. S11,S12). The mean and variance of the simulated sideward displacements using the best-fit parameters are plotted in Fig. 3 as dotted and solid lines; an exemplary stepping trace is

Table 1. Best-fit simulation parameters with standard deviations (SD, $N = 95$).

$x_l^\dagger$	$x_r^\dagger$	k_l^0	k_r^0
$3.6 \pm 0.8\,\text{nm}$	$2.5 \pm 1.0\,\text{nm}$	$0.31 \pm 0.03\,\text{s}^{-1}$	$0.28 \pm 0.04\,\text{s}^{-1}$

plotted in Fig. 4D. The simulated trace shows the counterintuitive effect that the sideward displacement y may be positive, close to zero, or negative even though the angular position always changes in the same direction with the same magnitude (see angular steps at $\approx 2\,$s, $3\,$s, and $5\,$s in Fig. 4D). Overall, the simulation fits the experimental data very well, supporting our diffusive, asymmetrically, force-biased stepping model.

1 Discussion

Our experiments have shown that (i) Kip3 motor-attached microspheres moved on average sidewards in the direction of load, (ii) the variance of the sideward displacement distribution increased with increasing sidewards pulling time, and (iii) detected individual sidewards steps had a broad distribution both in the direction of applied load and against it. While the latter two points are indicative of a diffusive process, the geometry may also be the cause for apparent bidirectional microsphere steps for a unidirectional, i.e. directed angular motion of the motors. However, such unidirectional motion is inconsistent with the load-induced sideward motion and steric hindrance. For a unidirectional angular motion, the motor would have to pass through underneath the microtubule, which is sterically impossible due to the attached microsphere.

Why do the mean and variance of the sideward displacement distributions saturate or even decrease for long alternating times? The geometry of the experiment explained the broad distribution in sideward step sizes and sideward distances. Moreover, because of the geometry, in addition to the force-dependent sideward stepping rates, we expect that for long alternating times the motor should on average localize to the protofilament oriented at the angle ϕ_{max}, for which the tangential force is zero (Fig. 4C). For deviations away from this angular position, the tangential force exponentially increases the counteracting sideward stepping rate while exponentially decreasing the rate in the direction pointing away from ϕ_{max}. Therefore, after a transient, the microsphere position should fluctuate around the position $y(\phi_{\text{max}})$. For long alternating times, the transient displacement to reach ϕ_{max} contributes little to the linear-fit based sideward displacement (as de-

fined in Fig. 2B) resulting in an overall mean sideward displacement Δy approaching zero. Since the force dependence of the leftward rate is larger, we expect that the mean angular position ϕ_{max} is reached faster compared to the right. Therefore, the transient is shorter and contributes less to the mean sideward displacement. The smaller contribution results in an overall smaller absolute mean sideward displacement to the left compared to the right. Thus, the dynamics of the system causes a larger mean displacement to the right, even though the leftward stepping rate is more sensitive to force. For long alternating times, we expect the variance to approach a constant value resulting from the fluctuations around the mean angular position. Taken together, our model is consistent with all of our experimental observations.

We assumed that the normal force did not affect the sideward stepping. Yet, we observed that the sideward load slowed down the forward motion. We attribute this slowdown to the normal force acting on the motor. To support this notion, we measured the forward speed while pulling upward on the motor (red open diamonds, top axis in Fig. 1C). We scaled the upward force axis relative to the sideward force axis by dividing the latter by $\cos(\phi_{max})$, which corresponds to the normal load force expected according to our model under sideward pulling conditions after the transient. With such a scaling, the data overlap: within error bars the decrease in forward speed upon upward loading suggests that the normal load is the key parameter that slows down the forward motion of the motor. While we could not measure any limping, we would expect the motor to limp with increasing sideward and normal loads.

For a single motor, our model suggest a purely diffusive sideward motion in the absence of loads with about every ninth step ($[2k_0 + k_f]/(2k_0) = [0.6 + 5]/0.6 \approx 9$) of the motor being a sideward step in a random direction. However, microtubule rotations observed in gliding assays suggested a leftward bias of the steps (22). According to our model, this leftward bias is due to the different force dependence of the sideward stepping rates (Table 1). The molecular origin of this difference may be due to the asymmetric structure of the kinesin head with respect to the neck linker (22). In the gliding assays, multiple motors operate together. Because motors do not step in synchrony, more advanced motors should apply loads on lagging ones. Since motors are attached to various angular positions on the microtubule, these loads have both a component in the direction of the microtubule axis and perpendicular to it causing tangential forces on the motor. Because of the asymmetric force-bias in the sideward stepping rates, the *ensemble* of motors should on average step to the left consistent with the

gliding assays (see Fig. S13 and Sect. S12). A similar collective effect has been observed for dynein (17), suggesting that dynein may also have a difference in the force dependence of the sideward stepping rates. Kip3 has a weakly bound slip state (28). The motor switches to this short-lived state at a frequency comparable to the sideward stepping rate. Whether sideward stepping is related to this state is unclear at the moment. A weakly bound state may enable the motor a longer reach to binding sites on neighboring protofilaments (22). Whether sideward stepping is coupled to ATP hydrolysis and how the sideward stepping rate depends on the ATP concentration is also unclear. We tested trapping assays at reduced ATP concentrations. However, a quantitative analysis of these assays turned out to be nearly impossible due to very low motor speeds and a seemingly reduced stall force. If sideward stepping is coupled to ATP hydrolysis, we would expect a small zero-force asymmetry in the sideward stepping rates, which we could not determine within our error margins. Such an asymmetry should arise because of the helical microtubule geometry and the asymmetry of the motor (22).

What biological relevance does the diffusive sideward stepping mechanism have for Kip3? For axonemal dynein motors, off-axis movement—causing microtubule rotations and, thus, torque—may be important for the three-dimensional motion of the flagellar beat (12, 13); for cytoplasmic dynein, sideward steps may be an essential biological requirement such that heads can pass each other, obstacles, or counter-propagating kinesin motors (15–17, 40). For kinesin motors, the ability to bypass obstacles is also an essential property for cargo transport (41–43). How torque generation (12, 13, 18–21) on the cargo, i.e. a rotation of the cargo around the filament axis, induced by sideward stepping influences cargo transport remains to be seen. Kip3 does not transport cargo, but must reach the microtubule end for length regulation. Therefore, being able to bypass obstacles on both sides seems to be the most efficient way to do so. The asymmetric force bias may not have a biological function for Kip3.

Supporting Material

Supporting material is available at
www.biophys.org/biophysj/supplemental/S0006-3495(XX)XXXXX-X.

Author contributions

M.B. performed measurements and analyzed the data, E.S. and M.B. developed the model and wrote the manuscript, E.B. programmed the simulation routine.

Acknowledgments

Supporting Citations

Reference (44) appears in the Supporting Material.

References

1. Howard, J., 2001. Mechanics of Motor Proteins and the Cytoskeleton. Sinauer Associates, Inc.

2. Svoboda, K., C. F. Schmidt, B. J. Schnapp, and S. M. Block, 1993. Direct observation of kinesin stepping by optical trapping interferometry. *Nature* 365:721–727.

3. Asbury, C. L., A. N. Fehr, and S. M. Block, 2003. Kinesin Moves by an Asymmetric Hand-Over-Hand Mechanism. *Science* 302:2130–2134.

4. Yildiz, A., M. Tomishige, R. D. Vale, and P. R. Selvin, 2004. Kinesin walks hand-over-hand. *Science* 303:676–678.

5. Schief, W. R., R. H. Clark, A. H. Crevenna, and J. Howard, 2004. Inhibition of kinesin motility by ADP and phosphate supports a hand-over-hand mechanism. *Proc. Natl. Acad. Sci. U. S. A.* 101:1183–1188.

6. Ray, S., E. Meyhöfer, R. A. Milligan, and J. Howard, 1993. Kinesin Follows the Microtubule's Protofilament Axis. *J. Biol. Chem.* 121:1083–1093.

7. Nitzsche, B., F. Ruhnow, and S. Diez, 2008. Quantum-dot-assisted characterization of microtubule rotations during cargo transport. *Nat. Nanotechnol.* 3:552–556.

8. Fehr, A. N., C. L. Asbury, and S. M. Block, 2008. Kinesin steps do not alternate in size. *Biophys. J.* 94:L20–2.

9. Wang, Z. H., S. Khan, and M. P. Sheetz, 1995. Single cytoplasmic dynein molecule movements: Characterization and comparison with kinesin. *Biophys. J.* 69:2011–2023.

10. Yildiz, A., M. Tomishige, A. Gennerich, and R. D. Vale, 2008. Intramolecular Strain Coordinates Kinesin Stepping Behavior along Microtubules. *Cell* 1:1030–1041.

11. Nishizaka, T., T. Yagi, Y. Tanaka, and S. Ishiwata, 1993. Right-handed rotation of an actin filament in an in vitro motile system. *Nature* 361:269–271.

12. Vale, R. D., and Y. Y. Toyoshima, 1988. Rotation and translocation of microtubules in vitro induced by dyneins from Tetrahymena cilia. *Cell* 52:459–469.

13. Kagami, O., and R. Kamiya, 1992. Translocation and rotation of microtubules caused by multiple species of Chlamydomonas inner-arm dynein. *J. Biol. Chem.* 103:653–664.

14. Reck-Peterson, S. L., A. Yildiz, A. P. Carter, A. Gennerich, N. Zhang, and R. D. Vale, 2006. Single-molecule analysis of dynein processivity and stepping behavior. *Cell* 126:335–348.

15. DeWitt, M. A., A. Y. Chang, P. A. Combs, and A. Yildiz, 2012. Cytoplasmic Dynein Moves Through Uncoordinated Stepping of the AAA plus Ring Domains. *Science* 335:221–225.

16. Qiu, W., N. D. Derr, B. S. Goodman, E. Villa, D. Wu, W. Shih, and S. L. Reck-Peterson, 2012. Dynein achieves processive motion using both stochastic and coordinated stepping. *Nat. Struct. Mol. Biol.* 19:193–200.

17. Can, S., M. A. Dewitt, and A. Yildiz, 2014. Bidirectional helical motility of cytoplasmic dynein around microtubules. *eLife* 3:e03205.

18. Yajima, J., and R. A. Cross, 2005. A torque component in the kinesin-1 power stroke. *Nat. Chem. Biol.* 1:338–41.

19. Pan, X., S. Acar, and J. M. Scholey, 2010. Torque generation by one of the motor subunits of heterotrimeric kinesin-2. *Biochem. Biophys. Res. Commun.* 401:53–57.

20. Brunnbauer, M., R. Dombi, T.-H. Ho, M. Schliwa, M. Rief, and Z. Ökten, 2012. Torque Generation of Kinesin Motors Is Governed by the Stability of the Neck Domain. *Mol. Cell* 46:147–158.

21. Yajima, J., K. Mizutani, and T. Nishizaka, 2008. A torque component present in mitotic kinesin Eg5 revealed by three-dimensional tracking. *Nat. Struct. Mol. Biol.* 15:1119–1121.

22. Bormuth, V., B. Nitzsche, F. Ruhnow, A. Mitra, M. Storch, B. Rammner, J. Howard, and S. Diez, 2012. The highly processive kinesin-8, Kip3, switches microtubule protofilaments with a bias toward the left. *Biophys. J.* 103:L4–6.

23. Walker, R. A., E. D. Salmon, and S. A. Endow, 1990. The Drosophila claret segregation protein is a minus-end directed motor molecule. *Nature* 347:780–782.

24. Varga, V., J. Helenius, K. Tanaka, A. A. Hyman, and T. U. Tanaka, 2006. Yeast kinesin-8 depolymerizes microtubules in a length-dependent manner. *Nat. Cell Biol.* 8:957–962.

25. Gupta Jr., M. L., P. Carvalho, D. M. Roof, and D. Pellmann, 2006. Plus end-specific depolymerase activity of Kip3, a kinesin-8 protein, explains its role in positioning the yeast mitotic spindle. *Nat. Cell Biol.* 8:913–23.

26. Varga, V., C. Leduc, V. Bormuth, S. Diez, and J. Howard, 2009. Kinesin-8 Motors Act Cooperatively to Mediate Length-Dependent Microtubule Depolymerization. *Cell* 138:1174–1183.

27. Su, X., W. Qiu, J. Mohan L. Gupta, J. B. Pereira-Leal, S. L. Reck-Peterson, and D. Pellman, 2011. Mechanisms Underlying the Dual-Mode Regulation of Microtubule Dynamics by Kip3/Kinesin-8. *Mol. Cell* 43:751–763.

28. Jannasch, A., V. Bormuth, M. Storch, J. Howard, and E. Schäffer, 2013. Kinesin-8 Is a Low-Force Motor Protein with a Weakly Bound Slip State. *Biophys. J.* 104:2456–2464.

29. Bormuth, V., V. Varga, J. Howard, and E. Schäffer, 2009. Protein friction limits diffusive and directed movements of kinesin motors on microtubules. *Science* 325:870–873.

30. Bormuth, V., J. Howard, and E. Schäffer, 2007. LED illumination for video-enhanced DIC imaging of single microtubules. *J. Microsc.* 226:1–5.

31. Trushko, A., E. Schäffer, and J. Howard, 2013. The growth speed of microtubules with XMAP215-coated beads coupled to their ends is increased by tensile force. *Proc. Natl. Acad. Sci. U. S. A.* 110:14670–14675.

32. Bormuth, V., A. Jannasch, M. Ander, C. M. van Kats, A. van Blaaderen, J. Howard, and E. Schäffer, 2008. Optical trapping of coated microspheres. *Opt. Express* 16:13831–13844.

33. Rogers, K. R., S. Weiss, I. Crevel, P. J.Brophy, M. Geeves, and R. Cross, 2001. KIF1D is a fast non-processive kinesin that demonstrates novel K-loop-dependent mechanochemistry. *EMBO J.* 20:5101–5113.

34. Block, S. M., L. S. B. Goldstein, and B. J. Schnapp, 1990. Bead movement by single kinesin molecules studied with optical tweezers. *Nature* 348:348–352.

35. Schäffer, E., S. F. Norrelykke, and J. Howard, 2007. Surface Forces and Drag Coefficients of Microspheres near a Plane Surface Measured with Optical Tweezers. *Langmuir* 23:3654–3665.

36. Mahamdeh, M., and E. Schäffer, 2009. Optical tweezers with millikelvin precision of temperature-controlled objectives and base-pair resolution. *Opt. Express* 17:17190–17199.

37. Tolic-Norrelykke, S. F., E. Schäffer, J. Howard, F. Pavone, F. Jülicher, and H. Flyvbjerg, 2006. Calibration of optical tweezers with positional detection in the back focal plane. *Rev. Sci. Instrum.* 77:103101.

38. Mahamdeh, M., C. P. Campos, and E. Schäffer, 2011. Under-filling trapping objectives optimizes the use of the available laser power in optical tweezers. *Opt. Express* 19:11759–11768.

39. Block, S. M., C. L. Asbury, J. W. Shaevitz, and M. J. Lang, 2003. Probing the kinesin reaction cycle with a 2D optical force clamp. *Proc. Natl. Acad. Sci. U. S. A.* 100:2351–2356.

40. Dixit, R., J. L. Ross, Y. E. Goldman, and E. L. F. Holzbaur, 2008. Differential regulation of dynein and kinesin motor proteins by tau. *Science* 319:1086–1089.

41. Korten, T., and S. Diez, 2008. Setting up roadblocks for kinesin-1: mechanism for the selective speed control of cargo carrying microtubules. *Lab Chip* 8:1441–1447.

42. Dreblow, K., N. Kalchishkova, and K. J. Böhm, 2010. Kinesin passing permanent blockages along its protofilament track. *Biochem. Biophys. Res. Commun.* 395:490–495.

43. Hoeprich, G. J., A. R. Thompson, D. P. McVicker, and W. O. Hancock, 2014. Kinesin's Neck-Linker Determines its Ability to Navigate Obstacles on the Microtubule Surface. *Biophys. J.* 106:1691–1700.

44. Leduc, C., F. Ruhnow, J. Howard, and S. Diez, 2007. Detection of fractional steps in cargo movement by the collective operation of kinesin-1 motors. *Proc. Natl. Acad. Sci. U. S. A.* 104:10847–10852.

Supporting Material

The Kinesin-8 Kip3 Switches Protofilaments in a Sideward Random Walk Asymmetrically Biased by Force

Michael Bugiel,[1] Elisa Böhl,[1] and Erik Schäffer[1],*
[1]Cellular Nanoscience Group, Center for Plant Molecular Biology, Eberhard Karls Universität Tübingen, Tübingen, Germany
*Correspondence: Erik.Schaeffer@uni-tuebingen.de

Contents

List of Figures

S1. Kip3 slowed down upon sideward loading
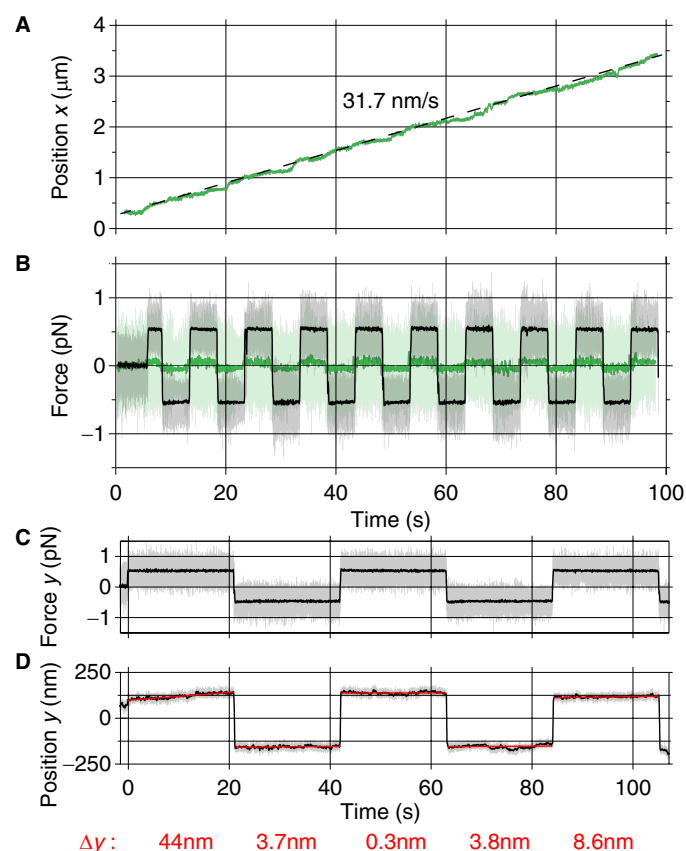
Fig. S1. (*A*) Trace of microsphere position (green line) along the microtubule axis (*x*-axis) as a function of time while subjected to alternating sideward loads of 0.5 pN with an alternating time of 5 s and no load applied along the microtubule axis. A linear fit (black dashed line) to the data resulted in a speed of ≈32 nm/s. (*B*) Corresponding force on the microsphere in the direction of the microtubule axis (*x*-axis, light green line: raw data with 4 kHz, dark green line: median filtered to 8 Hz) and perpendicular to it (*y*-axis, gray line: raw data with 4 kHz, black line: median filtered to 8 Hz) as a function of time. (*C*) Sideward load F_y and (*D*) microsphere position y for an alternating time of 21 s. Linear fits (red lines) and corresponding sideward displacements Δy are given.

S2. Kip3 sideward step dwell times are exponentially distributed
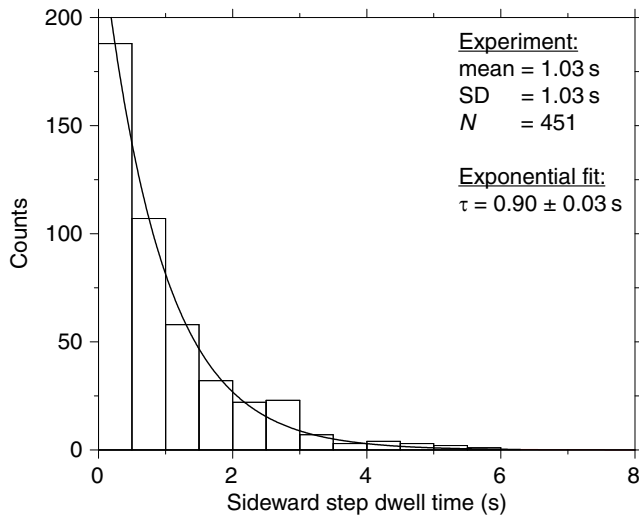
Fig. S2. Histogram of Kip3 experimental sideward step dwell times. An exponential (line) was fitted to the experimental data. The means, standard deviation (SD), and fitting result are given.

S3. Kip3 showed increasing mean sideward motion with increasing alternating times
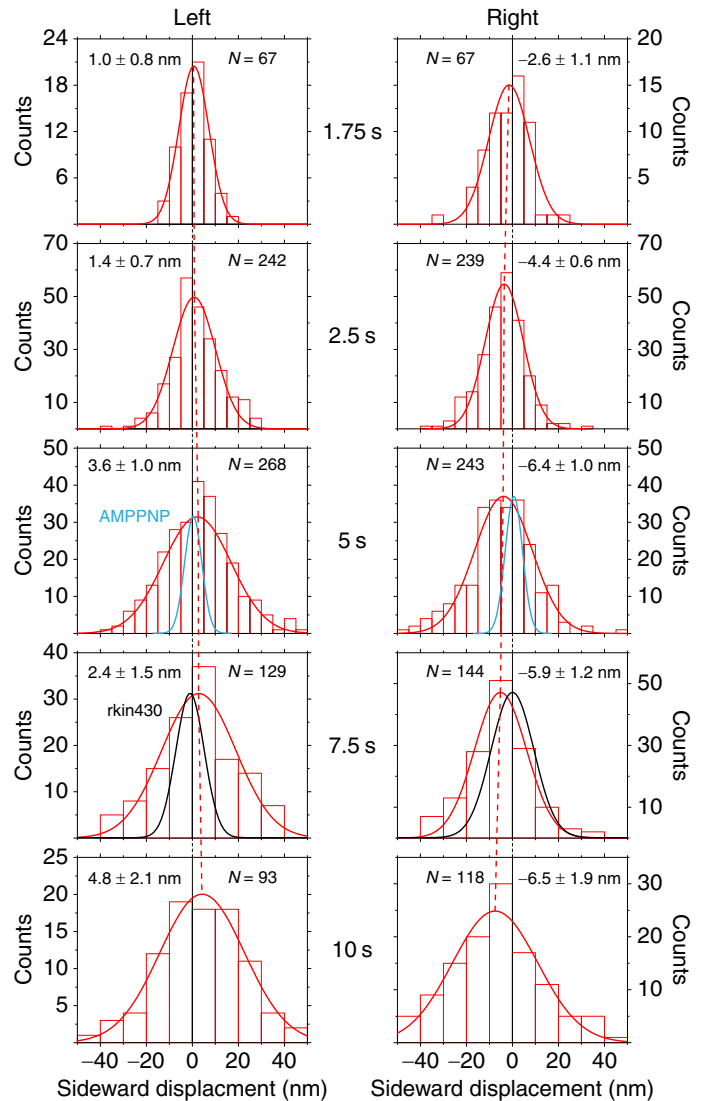
Fig. S3. Histograms and Gaussian fits (red lines) of sideward displacements Δy of motile Kip3 for a sideward load of 0.5 pN and alternating times of 1.75–10 s. Number N of evaluated alternating times, i.e. the number of measured Δy's and the mean±SEM are given. For comparison, Gaussian fits of AMPPNP-bound Kip3 (blue) for 5 s and rkin430 (black line) for 7.5 s, normalized to the same amplitude are plotted (see Figs. S4 and S5 for the corresponding data).

S4. Immotile kinesins showed no effective sideward motion

To determine our measurement precision, we applied sideward loads on immotile kinesins either in assay buffer containing the non-hydrolyzable ATP analog AMPPNP (Fig. S4A) or to pausing kinesins in the presence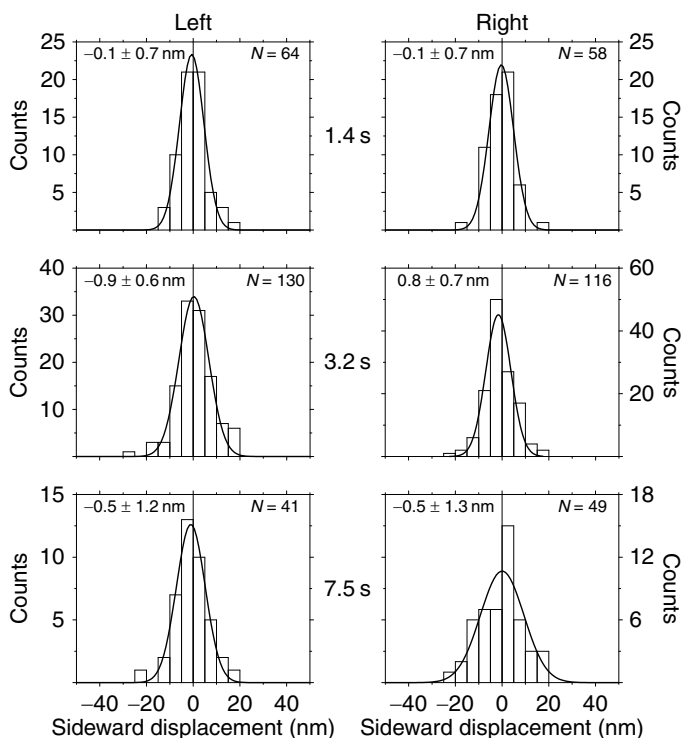 of ATP (Fig. S4B). Histograms of the sidewards displacements are plotted in Fig. S4C–H. For AMPPNP assays, loads (0.3–2.2 pN) were applied both parallel and perpendicular to the microtubule axis. Sideward displacements Δy were taken from 4 different microspheres (≥ 6 data points for several different forces in both directions). Since the motility direction was unknown, we defined Δy to be positive in the direction of load. T-tests ensured that the means for every force and direction were not significantly different from zero on the 95 % confidence level and thus consistent with each other (for one perpendicular force, the individual mean was significantly different from zero, but did not hold a Bonferroni correction). Therefore, all sideward displacements were plotted in one histogram for each direction (Fig. S4C, D). The mean values were less than 1 nm and not significantly different from zero. Because motors were not moving, we plotted the mean and variance of Fig. S4C in Fig. 3A and Fig. 3B, respectively, with an effective alternating time of zero. Also, for pausing kinesin motors the means were not significantly different from zero (Fig. S4E–H). The rare pausing events seemed to be related to the tubulin batch. They occurred in Kip3 as well in rkin430 assays, but less often with other tubulin preparations.

A AMPPNP, force and bead position

C AMPPNP, perpendicular

D AMPPNP, parallel

B Trace of pausing Kip3

E Kip3, pausing, left

F Kip3, pausing, right

G rkin430, pausing, left

H rkin430, pausing, right
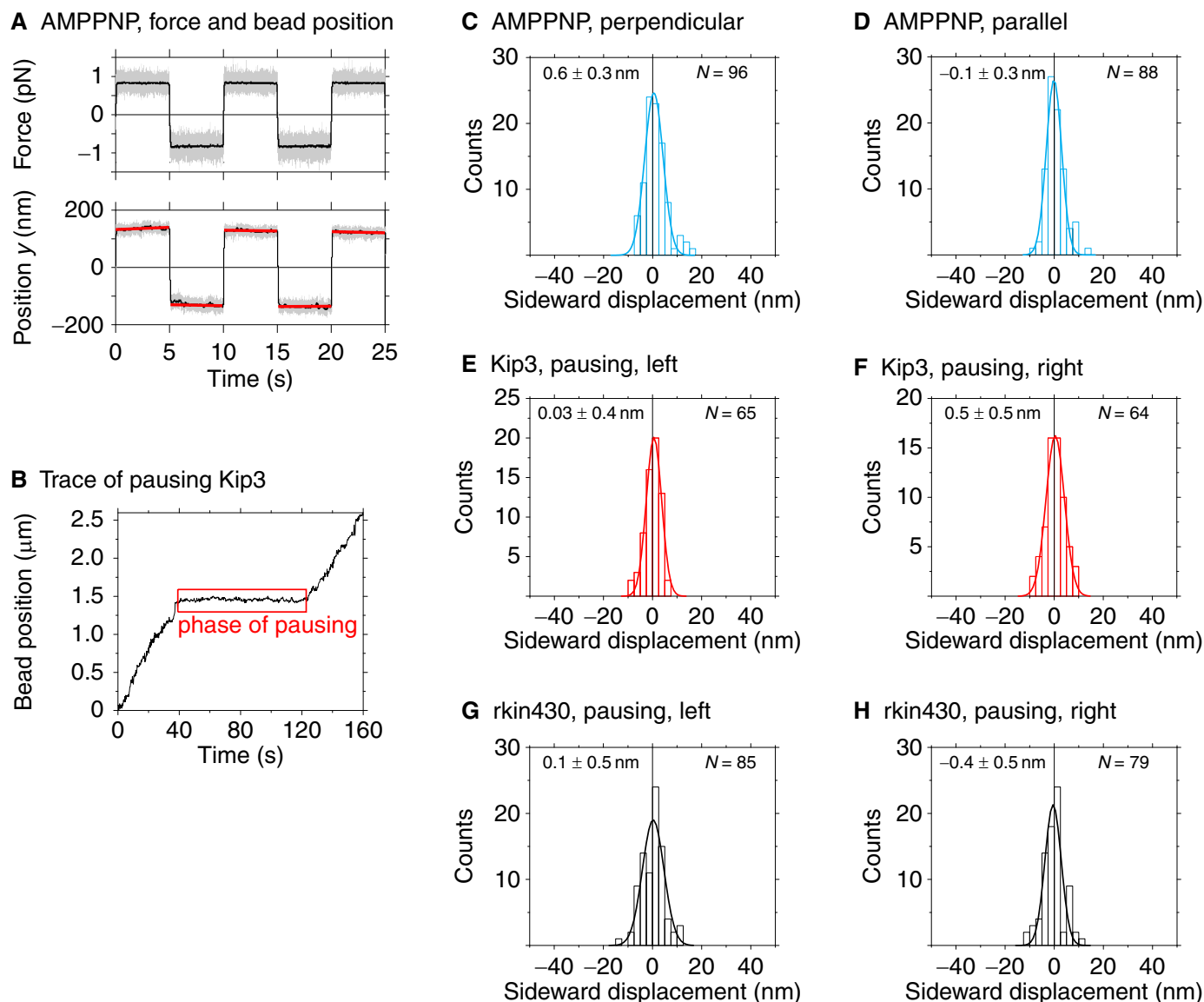
Fig. S4. (*A*) Force (top) and microsphere position (bottom) as a function of time of stationary Kip3 in the presence of AMPPNP under loads of ≈ 0.8 pN and an alternating time of 5 s including linear fits (red lines) to determine Δy. (*B*) Phase of pausing (≈ 80 s) for a non-trapped microsphere pulled by Kip3 and tracked via video microscopy. (*C–H*) Histograms with Gaussian fits of sideward displacements for (*C*) AMPPNP-bound Kip3, perpendicular to the microtubule axis, alternating time 5 s and (*D*) parallel to the microtubule axis, (*E*) pausing Kip3 with left and (*F*) right sideward loads of 0.5 pN pooled for various alternating times (1.75–20 s), (*G*) pausing rkin430 with left and (*H*) right sideward loads of 0.5 pN. Sample numbers N and means±SEMs are given.

S5. Kinesin-1 showed no effective sideward motion

To slow down kinesin-1 (rkin430-eGFP) to speeds comparable to Kip3, we reduced the ATP concentration in the buffer. With the reduced ATP concentration and four different experiments, the mean speeds were 21 ± 1 nm/s ($N = 45$), 28 ± 2 nm/s ($N = 58$), 37 ± 1 nm/s ($N = 36$) and 51 ± 2 nm/s ($N = 106$). The sideward load of 0.5 pN was alternated every 1.5–6 s. Longer alternating times were not feasible, as rkin430-coated microspheres detached on average before the end of the alternating time, consistent with kinesin-1's lower processivity compared to Kip3. We measured no decrease in the velocity due to the sideward loads. To compare the measured sideward displacements with those of Kip3, the alternating time t_{alt} was converted into an effective alternating time $t^{\text{eff}}_{\text{kinesin-1}}$, based on an equal number of forward steps on the microtubule lattice (equal distance): $t^{\text{eff}}_{\text{kinesin-1}} = t_{\text{alt}} \cdot v_{\text{kinesin-1}}/v_{\text{Kip3}}$. The effective alternating time of 0 s for AMPPNP-bound Kip3 in Sect. S4 was calculated the same way. For kinesin-1, the mean sideward displacements showed no increase over time for left nor right (Fig. 3A, histograms shown in Fig. S5). All means were statistically consistent with zero (confirmed by a χ^2-test). The weighted mean$\pm$SE over all alternating times was -0.1 ± 0.2 nm, indicating that kinesin-1 did not show any net sideward motion.

S6. Microtubule supertwist

Microtubules, grown in BRB80, MgCl$_2$, GTP and DMSO are built of 13–16 protofilaments with 14 occurring most often (1). The distribution of the number of microtubule protofilaments is given in Table S1. We assumed the same distribution in our microtubules. Note that the tubulin origin (porcine instead of bovine) was the only difference in the preparation of the microtubules compared to (1). Based on this distribution, we calculated a mean reciprocal supertwist pitch by weighting the reciprocal pitches in Table S1 according to their abundances. Thus, the mean reciprocal pitch was $0.126\,\mu\text{m}^{-1}$ corresponding to a mean pitch of $7.92\,\mu\text{m}$. On a 13 protofilament microtubule, such a pitch would correspond to one sideward step to the left for 76 forward steps. This results in a net leftward stepping rate of $0.05\,\text{s}^{-1}$ (assuming a forward stepping rate of $4\,\text{s}^{-1}$ at $F_y = 0.5$ pN). Since our measured sideward stepping rates were much higher, we do not expect that the supertwist had a significant influence on our measurements.

Table S1. Protofilament numbers, supertwist pitches, reciprocal pitches and abundances for microtubules, grown in BRB80, MgCl$_2$, GTP and DMSO. Left-handed supertwist pitches are denoted as positive and vice versa.

Proto-filament number	Supertwist pitch (1, 2)	Reciprocal supertwist pitch	Abundance (1)
	(μm)	(μm^{-1})	(%)
12	-3.4	-0.294	0
13	∞	0	14
14	7.75	0.129	72
15	3.3	0.303	11
16	∞	0	3

Fig. S5. Histograms and Gaussian fits (black lines) of sideward displacements Δy of motile kinesin-1 for a sideward load of 0.5 pN and different alternating times $t^{\text{eff}}_{\text{kinesin-1}}$. Sample numbers N and means$\pm$SEMs are given.

S7. Microsphere position vs. motor angle

According to the geometry illustrated in Fig. 4, the lateral microsphere center position $y(\phi)$ can be calculated from the angular motor position ϕ on the microtubule (MT) by

$$y(\phi) = \sqrt{(L + R)^2 - (R + h - r(1 + \sin \phi))^2} + r \cos \phi, \quad \text{(S1)}$$

where L is the linker length, R the microsphere radius, r the microtubule radius and h the height of the microsphere surface above the cover slip surface. Equation S1 has a maximum at $\phi_{\max} = \arcsin[(R + h - r)/(R + L + r)]$. Based on the geometry and orientation of the microtubule protofilaments, we can use Eq. S1 to estimate the mean sideward step size as measured by the microsphere (Fig. S6). This estimate is about twice as large compared to the projected distance between protofilaments and is used in the main text to calculate the sideward stepping rate based on the sideward diffusion coefficient.

Δp (nm)	0.7	3.4	5.3	6.0	5.3	3.4	0.7	2.1	4.5	5.8	5.8	4.5	2.1
Δy_s (nm)	-12.8	-6.7	-0.04	6.0	10.6	13.5	14.2	-9.9	-3.4	3.1	8.5	12.3	15.2
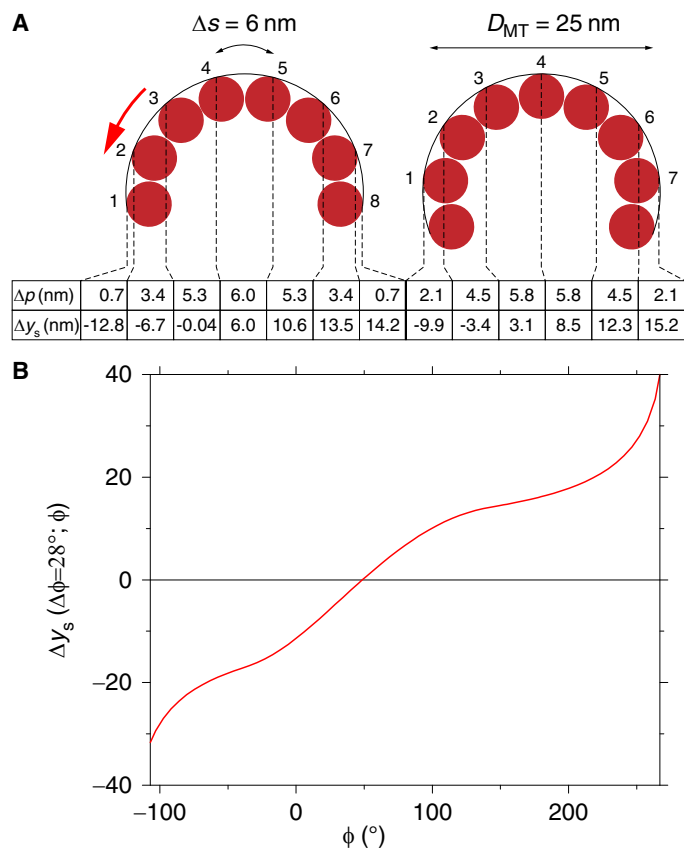
Fig. S6. (*A*) Upper half of a microtubule with a total of 13 protofilaments (red) in two angular orientations (left and right). Projected distance Δp between protofilaments and microsphere-measured sideward displacements Δy_s per sideward step to the left (red arrow). The average values for the two orientations are $\langle \Delta p \rangle = 3.8$ nm and $\langle \Delta y_s \rangle = 8.9$ nm. (*B*) Plot of Δy_s over a wide range of angular positions ϕ.

S8. Kip3 showed increasing mean sideward motion with increasing sideward loads
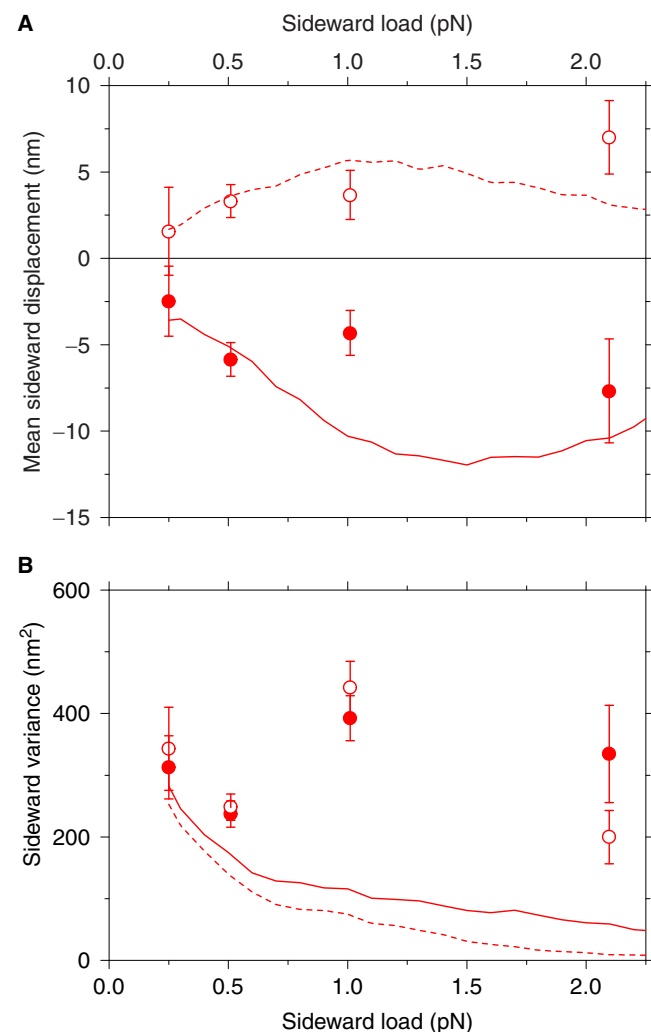
Fig. S7. (*A*) Mean sideward displacements and (*B*) sideward variances, depending on the applied sideward load for left (○) and right (●) loads for a constant alternating time of 5 s. Dashed and solid lines are the best-fit simulations for and left and right, respectively. Note that the force-dependent data point were not included to determine the best-fit parameters. The are calculated based on the best-fit simulation with fixed supertwist accounting for a force-dependent linker length (Fig. S10B). The predicted force dependence describes the data reasonably well (see Sect. S11 for more details).

S9. Vertical displacement during sideward pulling

0.1 ± 0.8 nm, $N = 138$
$t_{alt} = 10$ s
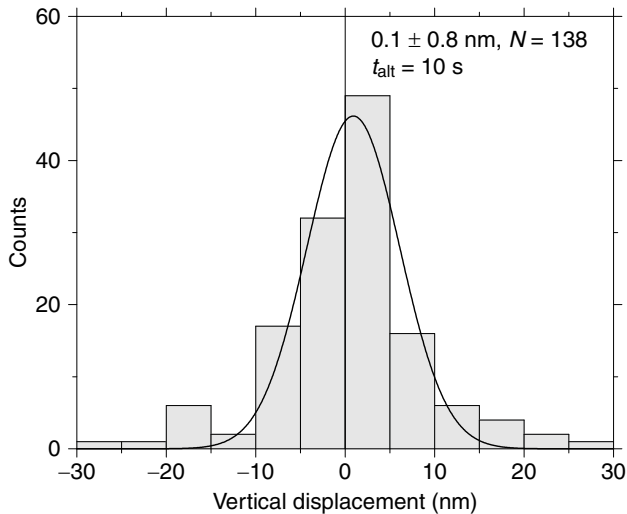
Fig. S8. Histogram of vertical displacements Δz with mean±SEM and Gaussian fit for an alternating time of 10 s.

S10. Details on the geometry

If a motor moves sideward beyond two critical angles ϕ_1^* and ϕ_2^*, the linker between the microtubule and microsphere starts to coil around the microtubule (Fig. S9A). If coiling occurs, we calculate the microsphere position based on a reduced linker length: $L(\phi) = L - r \cdot |\phi - \phi_{1,2}^*|$ for $|\phi| > |\phi_{1,2}^*|$. Note that the exact angular position of $\phi_{1,2}^*$ during coiling is not constant. However, the deviation from the initial value is negligible. The critical angles are given by:

$$\phi_{1,2}^* = \arcsin\left\{\frac{A(R+L) \pm r\sqrt{B-A^2}}{B}\right\} \mp \frac{\pi}{2}, \quad \text{(S2)}$$

where $A = R + h - r$ and $B = (R+L)^2 + r^2$. For the parameters we used ($R = 295$ nm, $L = 34$ nm, $h = 20$ nm (based on surface potential measurements with optical tweezers, described in (3)) and $r = 12.5$ nm), the critical angles are: $\phi_1^* = -21.0°$ and $\phi_2^* = 154.6°$ with the maximum angle being $\phi_{max} = 62.4°$. Accounting for coiling, the microsphere center position $y(\phi)$ as a function of the angular motor position ϕ is given by

$$y(\phi) = \begin{cases} \sqrt{C_1^2 - D_1^2} + r\cos\phi_1^* & \text{for } \phi < \phi_1^* \\ \sqrt{(L+R)^2 - E^2} + r\cos\phi & \text{for } \phi \in [\phi_1^*, \phi_2^*] \\ \sqrt{C_2^2 - D_2^2} + r\cos\phi_2^* & \text{for } \phi > \phi_2^*, \end{cases} \quad \text{(S3)}$$

where

$$C_i = R + L - r|\phi - \phi_i^*|$$
$$D_i = R + h - r(1 + \sin\phi_i^*)$$
$$E = R + h - r(1 + \sin\phi) \quad \text{(S4)}$$

with $i = 1, 2$. The coiling correction is a small correction for the microsphere displacements.

Coiling also affects the calculation of forces, which are defined in Fig. S9B. In the angular range without coiling of the linker, the tangential force on the motor—the force in the direction of sideward stepping—is given by $F_{tang} = F_{linker}\sin(\phi - \psi)$. The force in the direction of the linker is $F_{linker} = F_y/\cos\psi$, where F_y is the constant sideward load and ψ is the angle between linker and surface calculated according to

$$\psi(\phi) = \arcsin\begin{cases} D_1/C_1 & \text{for } \phi < \phi_1^* \text{ in radians} \\ E/(R+L) & \text{for } \phi \in [\phi_1^*, \phi_2^*] \\ D_2/C_2 & \text{for } \phi > \phi_2^*. \end{cases} \quad \text{(S5)}$$

For angles beyond the critical ones, the tangential force equals the linker force with reduced linker length. Thus, the tangential force is calculated by:

$$F_{tang}(\phi) = F_y\begin{cases} -1/\cos\left[\arcsin\psi(\phi)\right] & \text{for } \phi < \phi_1^* \\ \sin(\phi - \psi(\phi))/\cos\psi(\phi) & \text{for } \phi \in [\phi_1^*, \phi_2^*] \\ 1/\cos\left[\arcsin\psi(\phi)\right] & \text{for } \phi > \phi_2^*. \end{cases}$$
$$\text{(S6)}$$

Without coiling, the normal force on the Kip3 is calculated by $F_{norm} = F_{linker}\cos(\phi - \psi)$ and with coiling, the normal force is zero (see Fig. 4C)

$$F_{norm}(\phi) = F_y\begin{cases} 0 & \text{for } \phi < \phi_1^* \\ \cos(\phi - \psi(\phi))/\cos\psi(\phi) & \text{for } \phi \in [\phi_1^*, \phi_2^*] \\ 0 & \text{for } \phi > \phi_2^*. \end{cases}$$
$$\text{(S7)}$$

Based on the measured large, transient sideward displacements Δy_L and using the angular-motor-position to microsphere-position conversion equation Eq. S1, we can determine the linker length L under 0.5 pN load by

$$\Delta y_L = 2\sqrt{(L+R)^2 - (R + h - r(1+\sin\phi))^2}. \quad \text{(S8)}$$

We assumed that after sideward pulling, the motor has reached on average the angular position $\phi = \phi_{max}$. For this angle, we plotted the linker length L as a function of Δy_L (red line in Fig. S10A). Also plotted in Fig. S10A is the histogram of the large, transient displacements with a mean of $\Delta y_L = 305 \pm 2$ nm (SEM, $N = 509$). Graphically, the intersection of the mean with the red line resulted in the linker value of $L = 34 \pm 1$ nm, which we used in our calculations. This linker length is consistent with the expected length based on the length of the PEG linker, the GFP antibody, and Kip3 motor size. Analogously, the linker length for rkin430 for a sideward loads of 0.5 pN was $L = 52 \pm 1$ nm based on $\Delta y_L = 376 \pm 4$ nm ($N = 466$). The transient displacement Δy_L and linker length L as a function of the sideward load are plotted in Fig. S10B. The increase of Δy_L indicates a stretching of the protein/PEG linker.

S11. Simulations

Because of the geometry, it was impossible to find an analytical solution to the expected mean and variance of the sideward displacements. Therefore, we programmed a simulation routine in Java, based on the following model: Kip3 steps to the left, right, or forward with the zero-force
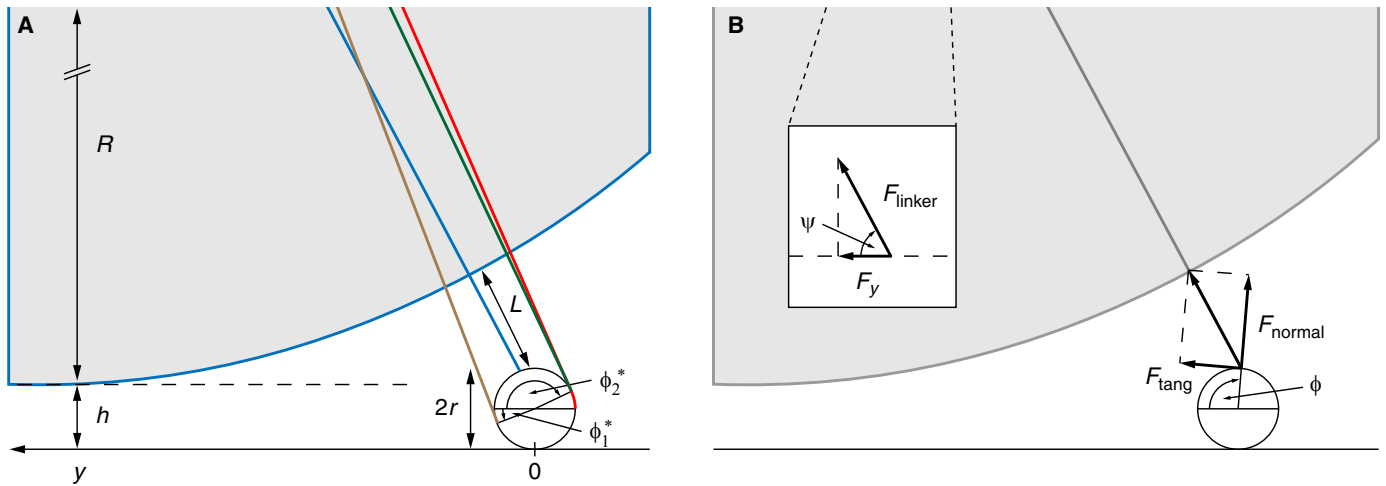
Fig. S9. (A) Schematic drawn to scale illustrating the critical angles and coiling of the linker if the motor moves sideward beyond the critical angles (brown: $\phi = \phi_1^*$, green and red, respectively: $\phi \geq \phi_2^*$). (B) Schematic of the tangential, linker, normal, and sideward load force.
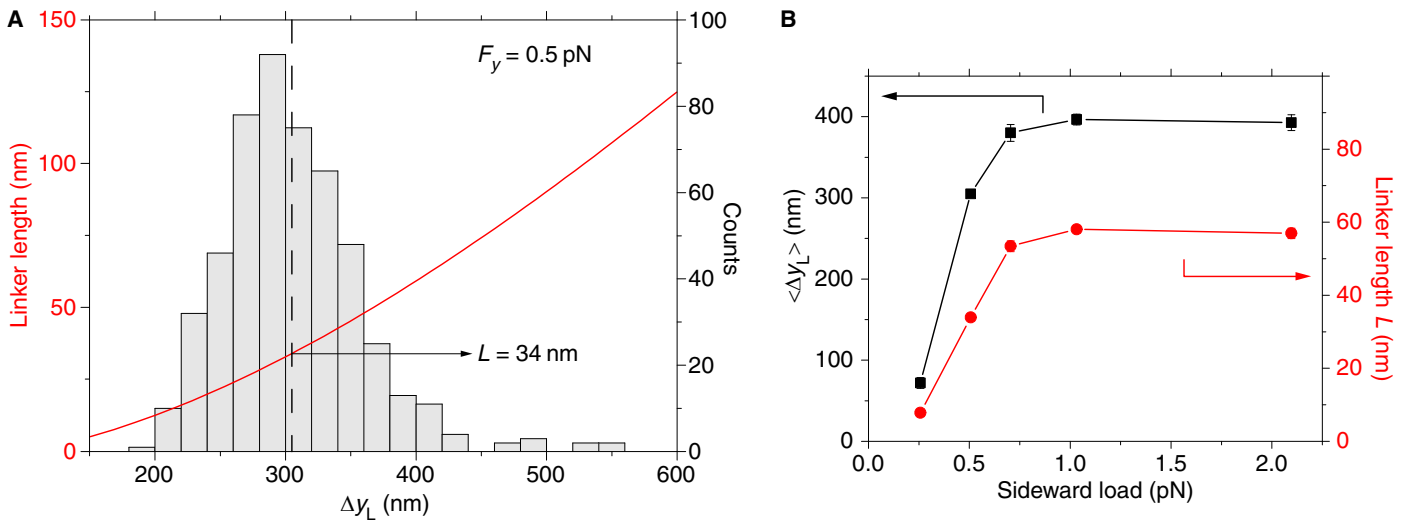
Fig. S10. (A) Linker length L (red line, left axis) as a function of large, transient sideward displacements Δy_L for a sideward load of 0.5 pN. Plotted is the inverse of Eq. S8 using $\phi = \phi_{max}$. The mean (dashed line) of the Δy_L histogram (right axis) intersects the red line at the linker length, we used for our calculations. (B) Mean transient displacements $\langle \Delta y_L \rangle$ (■) and corresponding linker length L as a function of the applied sideward load (●). Lines are guides to the eye.

rates k_l^0, k_r^0, and k_f, respectively. The side-stepping rates are influenced by an applied tangential load in an exponential manner:

$$k_{l,r}(F_{tang}) = k_{l,r}^0 \exp(\pm F_{tang} \cdot x_{l,r}^\dagger / k_B T). \tag{S9}$$

Thus, a positive tangential force $F_{tang} > 0$ to the left increases the stepping rate to the left and decreases the rate to the right. To account for the dependence of the Kip3 velocity on the sideward load, we used a forward stepping rate of $31.5\,\mathrm{nm\,s^{-1}} / 8\,\mathrm{nm} = 3.9\,\mathrm{s^{-1}}$ corresponding to the measured mean forward velocity. In the simulation, Kip3 performed a random walk on a cylinder with angular steps of $\delta\phi_{pf} = \pm 27.7°$ (the angle between neighboring protofilaments in a 13 protofilament microtubule) and forward steps of 8 nm (the distance between kinesin binding sites on a protofilament (4)). Because of the supertwist and the small relative displacements of neighboring protofilaments, a forward step was associated with a small angular displacement. Similarly, a sideward step

was coupled to a small forward displacement corresponding to the geometry of a microtubule with a supertwist pitch P. The control experiment with rkin430 was simulated without sideward steps and a constant forward stepping rate.

First, we simulated the forward stepping motion with an exponential distribution for the step duration with a mean of k_f^{-1} assuming that forward and sideward stepping are uncorrelated. Subsequently, we simulated and superimposed the sideward stepping motion. The probability of stepping to the left and right was calculated by the ratio of the corresponding rate to the sum of rates

$$P_{l,r} = \frac{k_{l,r}}{k_l + k_r}. \tag{S10}$$

The duration of sideward steps were chosen to be also exponentially distributed with a mean dwell time of $(k_l + k_r)^{-1}$. An exponential distribution is consistent with our measurements (Fig. S2). The angular starting position on the microtubule
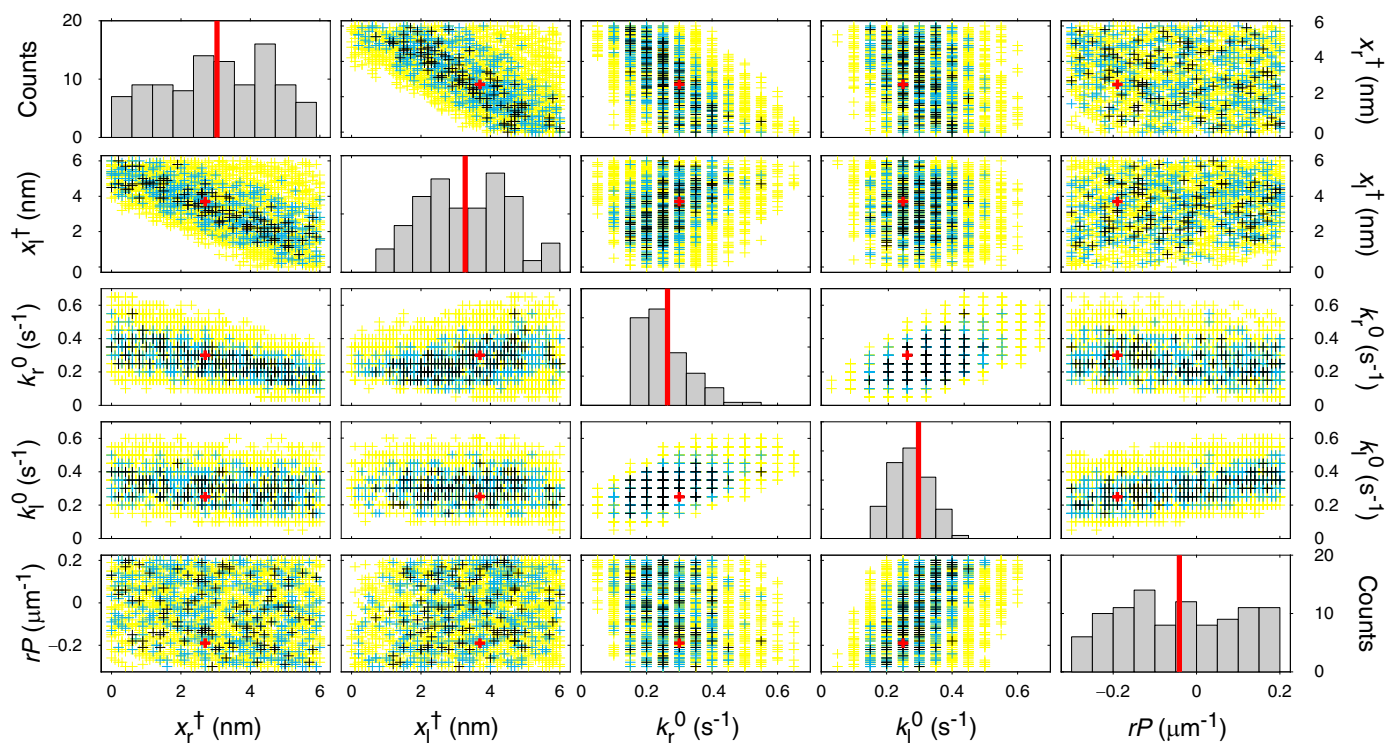
Fig. S11. Plots of parameter sets for $k_l^0, k_r^0, x_l^\dagger, x_r^\dagger$ and rP as a free parameter, plotted against each other. Red: best parameter set, black: best 100, blue: best 500, yellow: best 2500 parameter sets. Histograms with means (red bars) of the best 100 parameter sets are shown in the diagonal.
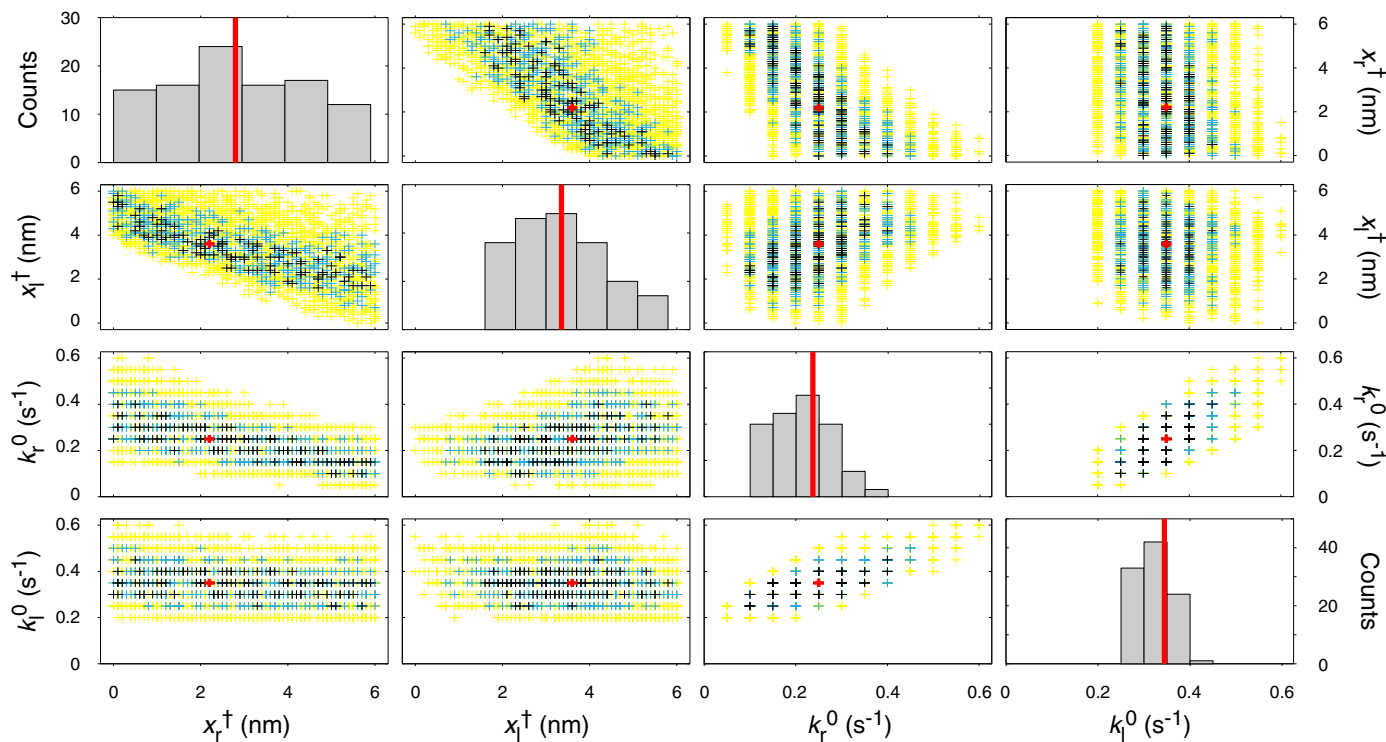
Fig. S12. Plots of parameter sets for $k_l^0, k_r^0, x_l^\dagger, x_r^\dagger$, plotted against each other. rP is fixed to a value of 0.126 μm^{-1}. Red: best parameter set, black: best 100, blue: best 500, yellow: best 2500 parameter sets. Histograms with means (red bars) of the best 100 parameter sets are shown in the diagonal.

Table S2. Average number of alternating times N, i.e. switches of load direction, per trace and number of used microtubules (MT) for different alternating times t_{alt} and different sideward loads F_y for all kinesin side-stepping assays. The total number of different microtubules used is indicated. Note that the same microtubules have been used for multiple alternating times.

Kip3						rkin430			
$F_y = 0.5\,\text{pN}$			$t_{\text{alt}} = 5\,\text{s}$			$F_y = 0.5\,\text{pN}$			
t_{alt} (s)	N	MT	F_y (pN)	N	MT	t_{alt} (s)	$t_{\text{kinesin-1}}^{\text{eff}}$ (s)	N	MT
1.75	18	15	0.25	10	13	1.6	1.4	16	12
2.5	14	38	0.5	12	61	1.5	2.4	14	26
5	12	61	1	16	8	4.0	2.6	14	14
7.5	10	39	2.1	8	6	4.9	3.2	12	20
10	6	50		**Total:**	88	2.5	4.1	12	22
15	4	53				7.0	6.2	8	8
20	2	44				5.3	6.2	6	2
	Total:	164				4.7	7.5	6	10
								Total:	57

was chosen randomly between 0 and 180°. The number of alternating times per trace were chosen to be the same as in the experiments (Table S2). For alternating times between the experimental ones, interpolated even values were used. After a switch, i.e. a change in sideward loading direction, the last angular position was set as the new starting position.

Since for every step, the angular position ϕ changed, we calculated and updated for every step the microsphere displacement $y(\phi)$, the tangential force $F_{\text{tang}}(\phi)$, the force dependent rates, the corresponding sideward stepping probabilities and step durations. Because the number of alternating times were equal to the experimental ones, the simulated traces also had the same overall durations. Additionally, we added normally distributed noise with a standard deviation of 3 nm corresponding to the experimental value of 12 nm, filtered down to the simulated sampling rate of 20 Hz. For each experimental alternating time, we simulated and analyzed 200 traces. Sideward displacements Δy and their means and variances were calculated from these traces in the same manner as for the experimental data.

We accounted for additional experimental noise—e.g. due to remnant mobility of microtubules, which showed up in the variance data, in particular for kinesin-1—by a global (fitting to both Kip3 and rkin430 data simultaneously) linear fit to the difference between the experimental variance and the simulated variance. The best linear fit was added to the simulated variance data of both motor types. We attribute the additional measurement noise to translocating motors. This noise may be caused, for example, by lateral motion of the antibody-surface-attached microtubule track. In extreme cases, we observed such motions by eye in the video images recorded during the experiments. The data from those extreme traces was not used for analysis. Such motions should depend on the position along the microtubule and should increase with larger distances covered on the microtubule track (see top axis of Fig. 3) resulting in an increased variance with the alternating time.

Without the linear fit parameters, the simulation had 5 free parameters: $k_l^0, k_r^0, x_l^\dagger, x_r^\dagger$, and the supertwist pitch P. Note that for the simulations, we used the reciprocal of the pitch rP, which we limited to a reasonable range (see Sect. S6) for different protofilament numbers. The side-stepping rates were randomly chosen with increments of $0.05\,\text{s}^{-1}$, the distance to the transition states with 0.1 nm increments, and the reciprocal supertwist pitch with $0.01\,\mu\text{m}^{-1}$ increments. Each simulation

set included more than 100 000 different parameters sets.

To find the best-fitting set of parameters, we calculated for each parameter set the χ^2-value, based on the difference between experimental and simulated mean sideward displacements and sideward variances of Kip3 weighted by the experimental error bars. In the first set of simulations, we varied all parameters randomly. For this set, we found that the value of rP did not converge to a best-fit value of χ^2, i.e. the value of the supertwist had little influence on the overall best-fit (Fig. S11). Also, the amplitude of the mean sideward displacement for the kinesin-1 simulation was always less than a nanometer for all values of the supertwist. These small values indicate that even for the protofilament tracker kinesin-1 the supertwist did not lead to any mean sideward displacements that should be detected by the experiment. Therefore, for the second set of simulations, we fixed the rP-value to the expected weighted mean value (Sect. S6). The simulation results are shown in Fig. S12. We used the corresponding best parameter set to simulate the force-dependent measurement. For this simulation, we used the load-dependent linker lengths L, given in Fig. S10B. The simulation results are shown in Fig. S7. For both sets, the best-fit parameters are shown in Table S3. Because the simulations correspond to independent experiments, we calculated the weighted means and SDs of the parameters, which are the values stated in the main text. The corresponding Pearson's correlation coefficients for the two simulations are given in Table S4.

S12. A model for gliding assays accounts for the rotation direction

We developed a simple model according to which the asymmetric bias in the force dependence is sufficient to explain the observed rotation direction in gliding assays. The model is based on the mutual influence that multiple motors in a gliding assay geometry have on each other. For the gliding assays, in analogy to our loading experiments, we expect, after a transient phase, that all motors should on average be located at an angular position for which the tangential force for each individual motor should be zero (see main text for an explanation and Fig. S13 for an illustration). For simplicity, let us consider the case of two motors. If both motors are initially in a state without tangential forces and one of the motor takes one sideward step, this motor causes a tangential force. The

Table S3. Best-fit results with standard deviations of kinetic parameters and reduced χ^2 values for simulations with fixed and free supertwist pitch rP. The bottom line contains weighted means and SDs of the two parameters sets. Note: χ^2_{red} includes only Kip3 data. The SD reflects the spread in parameters of simulations with a χ^2-value range that contains 97% of the probability distribution of the parameters. The number of simulations that were used for the SD calculations were 18 and 77 with 22 and 23 degrees of freedom, respectively.

	$x_l^\dagger$	$x_r^\dagger$	k_l^0	k_r^0	slope	intercept	χ^2_{red}
	(nm)		(s^{-1})		(nm^2/s)	(nm^2)	
rP free	3.7 ± 1.2	2.7 ± 1.4	0.25 ± 0.06	0.30 ± 0.05	5.8 ± 0.2	21.6 ± 0.3	1.48
rP fixed	3.6 ± 1.0	2.2 ± 1.6	0.35 ± 0.04	0.25 ± 0.07	5.6 ± 0.3	21.9 ± 0.3	1.43
mean±SD	3.6 ± 0.8	2.5 ± 1.0	0.32 ± 0.03	0.28 ± 0.04	5.7 ± 0.2	21.7 ± 0.2	

Table S4. Pearson correlation coefficients between the fitted parameters for the best 100 parameter sets of the two simulations.

	rP free					rP fixed			
	$x_l^\dagger$	$x_r^\dagger$	k_l^0	k_r^0	rP	$x_l^\dagger$	$x_r^\dagger$	k_l^0	k_r^0
$x_l^\dagger$	1	-0.9	-0.7	-0.3	-0.2	1	-0.9	-0.8	-0.3
$x_r^\dagger$	-0.9	1	0.6	0.1	0.1	-0.9	1	0.6	-0.0
k_l^0	-0.7	0.6	1	0.4	-0.2	-0.8	0.6	1	0.7
k_r^0	-0.3	0.1	0.4	1	0.7	-0.3	-0.02	0.7	1
rP	-0.2	0.1	-0.2	0.7	1				
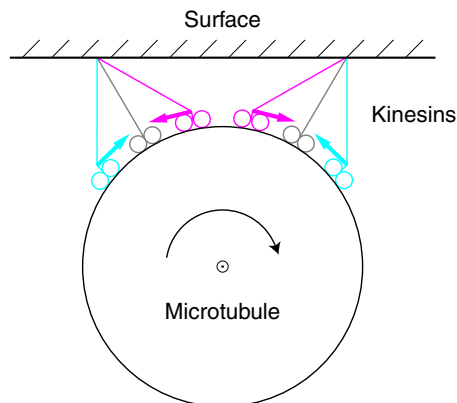
Fig. S13. Schematic of multiple motors interacting with a gliding microtubule moving out of the image plane leading to a clockwise rotation, i.e. the motors step on average to the left. Two motors are drawn in three different states (magenta, cyan, gray). Magenta and cyan colored motors symbolize the two different cases for which the tangential force (arrows) points in opposite directions. For gray motors, the tangential force is zero (see text for more details).

microtubule should rotate to a new angular position that distributes the tangential loads equally on both motors in analogy to the fractional steps observed for cargo transport driven by multiple motors (5). Since the motor can either step left or right with equal probability in the absence of a tangential force, there are two cases of loading directions illustrated by the magenta and cyan motors in Fig. S13.

Because of symmetry, the magnitude of the tangential forces on both motors should be equal. However, because of the asymmetric force bias, the leftward stepping rate should be on average larger compared to the right one, i.e. the exponential with the largest positive exponent should dominate the system. The force-induced difference between the left and right stepping rates should result in a net motor movement to the left for both of the above-mentioned cases. In the magenta case, on average, the left motor is most likely to take a step to the left. This stepping rate is the highest compared to any other stepping rate that either the left or the right motor have. In the cyan case, the right motor is most likely to take a leftward step. Thus, in both cases in the geometry of Fig. S13, which we expect to occur with equal probability, the net stepping rate toward the left should result on average in a clockwise rotation of the microtubule, which is the observed rotation direction in gliding assays (6). For more than two motors acting together, the force balance is difficult because it will depend on the individual location of all the motors. However, motors should still exert tangential forces onto each other, on average half of the motors should be to the left and right of the center, respectively, and the exponential with the largest positive exponent should dominate. Thus, also in this case we expect clockwise microtubule rotations and a net motor bias towards the left.

Supporting References

1. Ray, S., E. Meyhöfer, R. A. Milligan, and J. Howard, 1993. Kinesin Follows the Microtubule's Protofilament Axis. *J. Biol. Chem.* 121:1083–1093.
2. Nitzsche, B., F. Ruhnow, and S. Diez, 2008. Quantum-dot-assisted characterization of microtubule rotations during cargo transport. *Nat. Nanotechnol.* 3:552–556.
3. Schäffer, E., S. F. Norrelykke, and J. Howard, 2007. Surface Forces and Drag Coefficients of Microspheres near a Plane Surface Measured with Optical Tweezers. *Langmuir* 23:3654–3665.
4. Jannasch, A., V. Bormuth, M. Storch, J. Howard, and E. Schäffer, 2013. Kinesin-8 Is a Low-Force Motor Protein with a Weakly Bound Slip State. *Biophys. J.* 104:2456–2464.
5. Leduc, C., F. Ruhnow, J. Howard, and S. Diez, 2007. Detection of fractional steps in cargo movement by the collective operation of kinesin-1 motors. *Proc. Natl. Acad. Sci. U. S. A.* 104:10847–10852.
6. Bormuth, V., B. Nitzsche, F. Ruhnow, A. Mitra, M. Storch, B. Rammner, J. Howard, and S. Diez, 2012. The highly processive kinesin-8, Kip3, switches microtubule protofilaments with a bias toward the left. *Biophys. J.* 103:L4–6.